Journal of Materials Chemistry A

ROYAL SOCIETY OF CHEMISTRY

PAPER

View Article Online
View Journal | View Issue

Cite this: J. Mater. Chem. A, 2026, 14, 6003

Phonon RIXS signatures reveal polaron formation in oxygen redox Li- and Na-ion battery cathodes

Moritz Hirsbrunner, *[a] Pontus Törnblom,[a] Sahil Tippireddy,[b] Ke-Jin Zhou,[b] Mirian Garcia-Fernandez,[b] Robert A. House,[c] Håkan Rensmo[ad] and Laurent C. Duda *[a]

Received 19th September 2025
Accepted 27th December 2025

DOI: 10.1039/d5ta07689g

rsc.li/materials-a

Oxygen redox (OR) in $Li_{1.2}Ni_{0.13}Co_{0.13}Mn_{0.54}O_2$ and $Na_{0.67}Mg_{0.28}Mn_{0.72}O_2$ has been associated with the formation of embedded molecular O_2 due to the appearance of their distinctive features in RIXS, while it is unclear whether OR also affects the oxygen left in the lattice. Here we use high-resolution oxygen K-edge resonant inelastic X-ray scattering (RIXS) at threshold excitation (527.5–529.5 eV) revealing lattice responses due to OR. We find that both cathodes show pronounced multiphonon progressions, which are either altered or activated upon charging. The first progression, with a fundamental energy loss ~67–74 meV, matches the A_{1g} lattice-oxygen mode observed by Raman spectroscopy, confirming its bulk origin. The second progression that exhibits a fundamental loss of ~98 meV appears only at the highest state of charge and is resonant with the new pre-edge states at 527.5 eV. The latter mode emerges concurrently with the characteristic trapped-O_2 RIXS signal and is strongly coupled to an occupied electronic band near the Fermi level, indicating that OR may not only contribute to the formation of molecular O_2, but also perturbs lattice oxygen states, likely *via* polaron-forming oxidized lattice oxygen.

1 Introduction

Lithium-ion batteries dominate today's electrical energy-storage landscape from smartphones to electric vehicles and grid buffers, yet their practical capacity is still capped by the cathode.[1–4] One promising route to break this limit is oxygen redox in Li- and Na-based layered transition-metal oxides, whose extra capacity derives from reversible oxidation of lattice oxygen.[5–8]

Although oxygen redox (OR) has been widely studied,[9–15] its origin and microscopic mechanism remain not fully understood. Among the various spectroscopic probes, RIXS has delivered distinctive, chemical-specific evidence for trapped molecular O_2 in charged cathodes that become embedded in nanovoids[12] and has been corroborated using neutron scattering.[16] In contrast to this electrochemically formed O_2 in $Li_{1.2}Ni_{0.13}Co_{0.13}Mn_{0.54}O_2$ (LR-NMC) and $Na_{0.67}Mg_{0.28}Mn_{0.72}O_2$ (NMMO), certain other cathode systems[13] that are not considered to be true OR materials such as NMC-811 and LCO, surprisingly also exhibit this RIXS feature unless sufficient dose-reduction measures are taken, and it has been explained to be a consequence of X-ray irradiation.[13]

Upon discharge of the OR materials NMMO and LR-NMC, the O_2 signal diminishes and disappears, implying reduction and reincorporation into the oxide framework. How this molecular species forms and what role the bulk lattice oxygen plays is still unclear. Seo *et al.*[10] emphasized that oxygen redox should be viewed as the removal of electrons from non-bonding ("orphaned") O 2p states located just below the Fermi level. To date, however, RIXS has largely highlighted the embedded O_2 fingerprint, while leaving the intrinsic lattice response underexplored.

Vibrationally resolved RIXS (VR-RIXS) is uniquely suited to this task because it distinguishes oxygen species *via* their characteristic vibrational progressions.[17] Classical oxygen-redox cathodes exhibit two intense hallmark RIXS features at incident energies 531.0–531.5 eV: (i) a narrow peak at ~524 eV emission energy, and (ii) a series of gas-like vibrational losses extending 0–2 eV, both tracing the strong π^* resonance of trapped O_2. Additional progressions at higher excitation energies (>534 eV) have recently been assigned to minor hydroxide or carbonate products.[18] While important considering degradation aspects, they belong to irreversible by-products and thus provide limited insight into the details of reversible redox mechanism.

Reversible participation of lattice oxygen might rather manifest itself as empty states emerging right at the O K-edge threshold on charging, producing absorption features near 527.5–528.0 eV. Indeed, House *et al.*[17] reported such a pre-edge

[a]Condensed Matter Physics of Energy Materials, Division of X-ray Photon Science, Department of Physics and Astronomy, Uppsala University, Box 516, 751 20 Uppsala, Sweden. E-mail: laurent.duda@physics.uu.se; Tel: +46 18 4713512
[b]Diamond Light Source, Harwell Science and Innovation Campus, Fermi Ave., Didcot OX11 0DE, UK
[c]Department of Materials, University of Oxford, Oxford OX13PH, UK
[d]Wallenberg Initiative Materials Science for Sustainability, Department of Physics and Astronomy, Uppsala University, 751 20 Uppsala, Sweden

feature in charged $Na_{0.6}[Li_{0.2}Mn_{0.8}]O_2$, along with low-energy RIXS intensity that approaches the elastic line, consistent with delocalised O 2p holes in the lattice. A similar, distinct 527.5 eV pre-edge feature in charged $Na_2Mn_3O_7$ was interpreted by Abate *et al.*[19] as evidence of polaron formation involving localized O^- holes which form O–O dimers. Note that similar threshold broadening is observed for LR-NMC and NMMO, yet no high-resolution RIXS study has probed this region systematically.

In this work, we present a study focused on threshold-excited O K-edge VR-RIXS (527.5–529.5 eV) of LR-NMC and NMMO which represent prototypical Li- and Na-ion OR cathodes, respectively, dominated by O_2 formation. Nevertheless, two relatively intense phonon progressions are resolved both of which exhibit strong electron–phonon coupling: (a) a non-OR lattice mode at ∼70 meV and (b) an OR mode at ∼100 meV assigned to vibrations of polaron dimers formed by oxidized oxygen. Our investigation reveals a number of interesting observations. For one, vibrational signatures of lattice phonons in OR cathodes have been identified and analyzed for the first time. Additionally, polaron formation in layered OR cathodes has been detected and may play an important regulating role in OR mechanism. In a broader context, our investigation suggests that improved control over electron–phonon coupling, particularly in stabilizing oxygen hole polarons, could enable more effective design of these types of cathode materials.

2 Experimental

2.1 Sample synthesis and electrochemistry

The active material of LR-NMC was synthesized *via* sol–gel method following the procedure given in Luo *et al.*[11] In the case of NMMO, a solid-state reaction was utilized to synthesize the material with the full procedure described in Maitra *et al.*[20] Electrodes for subsequent galvanostatic cycling were prepared as a mixture of 80 wt% active material, 10 wt% carbon black, and 10 wt% polytetrafluoroethylene (PTFE) binder. The battery cycling was conducted *via* a Biologic VMP3 potentiostat, using half cells of synthesized electrodes with a Li/Na-metal counter electrode respectively, and 1 M LiPF6/NaPF6 (Alfa Aesar, ≥99.0%) in propylene carbonate (PC) as the electrolyte (BASF Selectilyte). The PC was dried for several days using molecular sieves (type 4 Å) prior to making the electrolyte. The two sample systems consist of pristine and charged samples in each case. For LR-NMC, the three chosen samples were: The pristine cathode material, a sample charged to the end of the plateau in the cycling curve, which corresponds to 0.8 lithium content per unit cell or a voltage of 4.3 V and finally a sample charged to 4.8 V. From here on, the three samples are denoted as 'pristine', end-of-plateau – 'EOP', and end-of-charge – 'EOC', respectively. For NMMO, two samples were chosen. The pristine cathode material (denoted as 'pristine') and a sample charged until 4.8 V (end-of-charge – 'EOC').

2.2 X-ray spectroscopy

The X-ray absorption spectroscopy (XAS) and RIXS measurements were conducted at beamline I21 at the Diamond Light Source in Oxfordshire, UK. A divergent variable line spacing grating is utilized in the RIXS spectrometer and beamline with an accessible energy range of 280–3000 eV. The samples were mounted on a He-cooled (T ∼15 K) precision-*xyz*-controlled manipulator. The spot size of the beam on the sample is approximately 40 × 2 μm^2 (h × v).[21] The movable spectrometer arm at I21 allows the investigation of varying scattering angles between incident and emitted photons. Horizontal polarization was used for all measurements and two scattering angles were compared (154° and 70°). The sample surface was angled at 45° and 30° towards the incoming beam respectively. The measurements from both angles are in close agreement (see SI Fig. S1–S3) and all graphs display data taken at 154° (reducing possible surface contributions and polarization effects). The resolution of the RIXS data obtained for this study was determined to be approximately 27 meV at 530 eV by analyzing the FWHM of the elastic peak which corresponds roughly to a resolving power of $E/\Delta E \approx 20\,000$. Note, however, that center of gravity determination of Gaussian-fitted peaks allows an accuracy of close to 1 meV.

The XAS spectra were obtained in total fluorescence yield mode (TFY), using a photodiode situated inside of the main experimental chamber. The XAS spectra are normalized to the end of each respective spectrum (560 eV).

Beam damage effects were evaluated by monitoring the evolution of RIXS spectra at various incident energies in 10 second increments for up to 10 minutes. No spectral changes were detected at any energy for the first few minutes (at least). While the presented spectra were recorded for 2.5 min per spot, comparison to spectra in continuous-movement mode showed that no detectable beam damage effects had evolved in this time frame.

2.3 Evaluating the electron–phonon coupling strength

To obtain the electron–phonon coupling (EPC) constants from the experimental data, software created by A. Geondzhian and K. Gilmore was utilized.[22] The software is designed to fit phonon contributions of experimental RIXS data and extract values for the electron–phonon coupling strength using three different models. A 1D displaced harmonic oscillator model, a 2D harmonic oscillator model considering two active phonon modes, and a 1D harmonic oscillator which is displaced and distorted in the excited state. The equations utilized for this fitting procedure are described by K. Gilmore[23] eqn (2) through (5) and are based on the work of L. J. P. Ament *et al.*[24] For the purpose of this work, the model based on the 1D displaced harmonic oscillator was utilized with the following fitting parameters: The electron–phonon coupling constant M_{epc} (eV), the energy of the oscillator ω_{ph} (eV), and half of the inverse phonon lifetime $\Gamma_{ph}/2$ (eV). At the same time the following parameters were kept constant, based on the experimental measurement conditions: the energy of the electronic excitation ($\omega_{ex} = 529.5$ eV), the energy of the incoming photon ($\omega_{in} = 529.5$ eV), half of the inverse core-hole lifetime ($\gamma/2 = 0.12$ eV), and the experimental broadening ($\alpha_{exp} = 0.027$ eV). Finally, the number of final and intermediate state oscillators were also fixed for the

fitting procedure at $n_f = 10$ and $n_m = 100$, respectively. The fitting procedure was constrained to the part of the spectrum representing phonon excitations and excludes the elastic peak, resulting in a range of 0.041 to 0.45 eV energy loss. The resulting RIXS spectra and fitted parameters are given in Fig. 5 and Table 2.

2.4 Raman spectroscopy

Raman measurements were conducted under argon atmosphere using a Raman Renishaw InVia spectrometer equipped with a diode laser with wavelength $\lambda = 785$ nm and 1.5 mW power.

3 Results and discussion

3.1 O K-edge X-ray absorption

Fig. 1 presents TFY O K-edge X-ray absorption spectra of NMMO and LR-NMC in three states of charge: pristine, EOP and EOC. Discussion is confined to the pre-edge window where oxygen-redox signatures emerge.

For LR-NMC a distinct shoulder appears around 528.5 eV upon reaching EOP (red difference trace in Fig. 1). Further charging does not amplify this feature; instead, intensity develops around 1 eV below, at 527.5 eV (blue difference trace). NMMO shows a smaller increase at 528.5 eV but likewise gains intensity at 527.5 eV once fully charged. Both oxides also exhibit the enhancement at *ca.* 531 eV that is indicative of trapped O_2.[17] In contrast to this extrinsic oxygen-redox signal, the new absorption structures at 527.5–528.5 eV are attributed to intrinsic lattice oxygen responses.

Three incident energies were selected for detailed vibrationally-resolved RIXS (vertical dashed lines in Fig. 1): 527.5, 528.5 and 529.5 eV, hereafter labelled excitation A, B, and C, respectively. Fig. 2 compares elastic-peak-subtracted O K-edge RIXS spectra recorded at excitations A–C (raw data in SI, Fig. S1). All spectra were normalized to the main emission band feature at ~4 eV. Low-energy loss peaks (<0.5 eV) form multi-phonon progressions while the main band ($\gtrsim$ 3 eV loss) evolves strongly with state of charge, indicating substantial electron–phonon coupling.

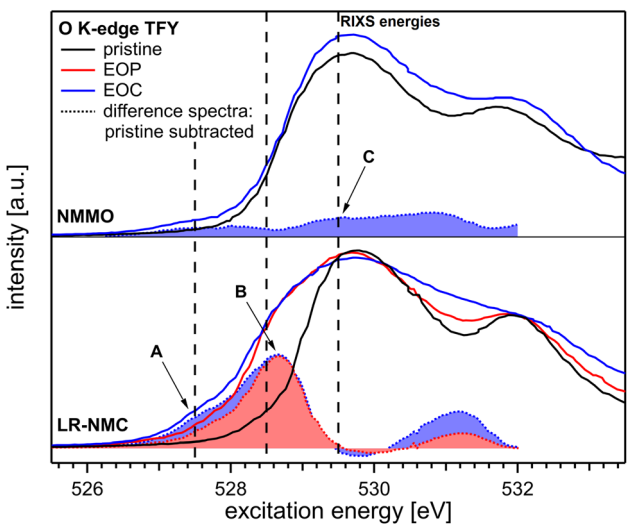

Fig. 1 O K-edge XAS of NMMO and LR-NMC at three different states of charge: pristine, EOP, EOC. The vertical dashed lines indicate at which energies RIXS spectra were obtained (527.5, 528.5, and 529.5 eV). The shown XAS spectra were obtained in TFY mode.

Angle dependent RIXS (SI Fig. S3) provides information about the transferred momentum dependence of collective excitations such as phonons even in the case of polycrystalline samples such as cathode materials. In a randomly oriented polycrystalline sample, acoustic phonons are expected to contribute predominantly to the low-energy continuum-like background starting at zero energy loss, rather than to the discrete, sharp peaks we associate with optical-multiphonon progressions. We observe in the energy loss region < 0.5 eV that discrete, sharp peaks ride atop a continuum type response starting from zero energy loss. There is no detectable momentum dependence between scattering angles 70° and 154° for the energy positions of the discrete peaks, which is typical for optical phonons. In contrast, the intensity variations of the spectra may at least partially be due to the momentum dependence of a background of acoustic phonons. The strongly increased background for excitation energy A compared to C for both NMMO and LR-NMC may well reflect the increased ratio of acoustic to optical phonons that couple to polarons. In the following, we will only address the multiphonon progressions that appear as sharp peaks in Fig. 2 and can be separated into two distinct manifolds, which becomes clearer in Fig. 3.

Progression I (68–84 meV), is present at excitation B and C for both pristine and charged (EOP and EOC) electrodes. Its energy matches the Raman-active A_{1g} lattice-oxygen breathing mode.

Progression II (98–99 meV) appears only at excitation A and only after deep charge (EOC). It grows in parallel with the extrinsic O_2 feature at 531 eV yet resonates 3–4 eV lower in incident energy, pointing to a different electronic origin.

Fig. 3a highlights the low-energy (0–0.37 eV) vibrational region of the O K-edge RIXS spectra for NMMO. Gaussian deconvolution reveals third- and fourth-order peaks, confirming genuine multiphonon behavior. The complete results of the fitting procedure are shown in the SI, Section 3. Focusing on excitation A, a pronounced difference emerges between the pristine and charged NMMO cathodes: the pristine sample lacks Progression II, while the charged sample shows distinct peaks at 98, 196, and 294 meV. At excitations B and C, the phonon signatures of Progression I shift slightly toward higher energy losses in the charged cathode. Specifically, the fundamental energies of Progression I blue-shifts from 71 meV (pristine) to 84 meV (charged) at B, and from 70 to 77 meV at C.

For LR-NMC (Fig. 3b), similar vibrational behavior is observed, though with notable contrasts. Progression I, seen at Excitation C, red-shifts upon charging from 75 to 73 meV opposite to the blue-shift seen in NMMO. This inversion highlights the sensitivity of phonon-RIXS to structural and redox-dependent variations. At excitation A, the pristine LR-NMC shows no strong vibrational features (while the electronic main band still shows a RIXS signal), whereas the EOC sample

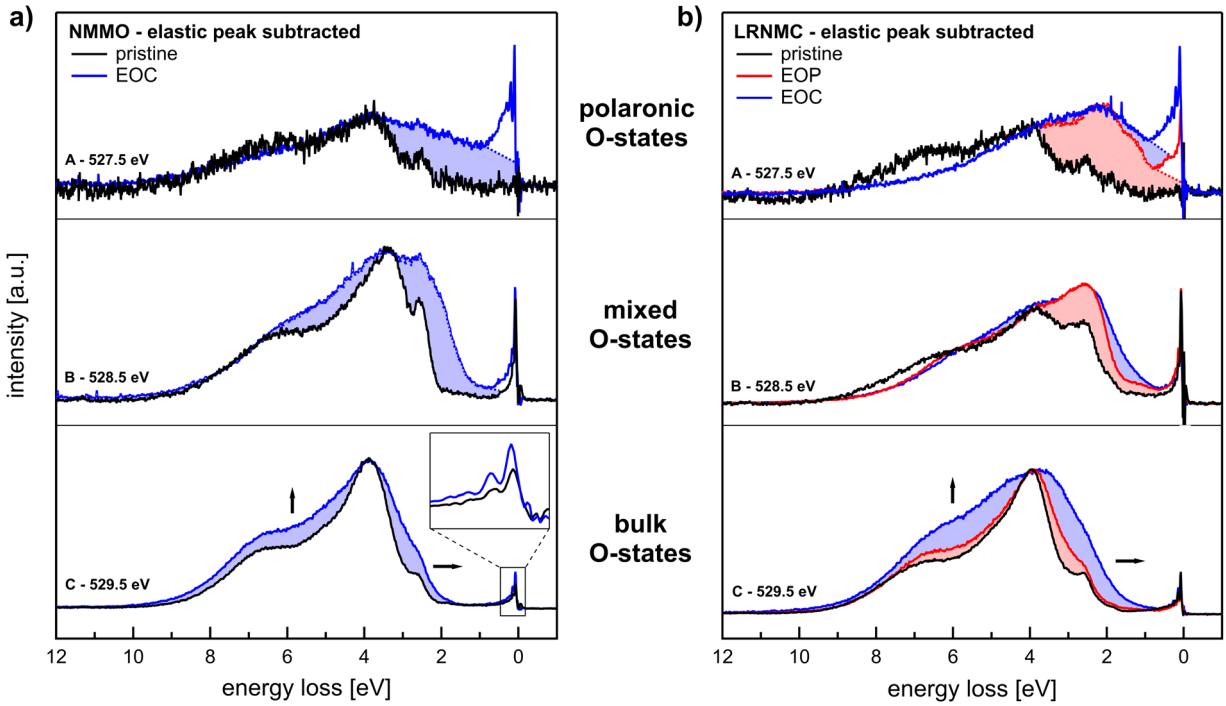

Fig. 2 O K-edge RIXS on NMMO (a) and LR-NMC (b) with the elastic peak subtracted *via* the procedure described in the SI (Fig. S4 in Section 2). The spectra are normalized to the main energy loss feature. Dashed lines in the vibrational peak energy region show the possible background of electronic states extended closer to the Fermi level (~0 eV). The inset in (a) shows an example of a blown up view of the low energy loss region for NMMO at excitation C.

exhibits a well-defined sequence, identified as Progression II at 99 meV. The EOP sample displays a broadened peak structure, likely a result of an overlap between Progression I and II in this partially charged sample. The lattice related Progression I vanishes for the EOC sample, indicating the formation of a new coupling mechanism in the fully delithiated state.

3.2 Origin of Progression I

The fundamental modes of Progression I in both NMMO and LR-NMC coincide in energy with the central region of the corresponding Raman spectra (Fig. 4), which exhibit a broad distribution of peaks between 300–700 cm^{-1} (37–87 meV). Due to differences in selection rules and transition matrix elements, the RIXS signal (despite having a lower energy resolution) seems to reflect a sub-set of these peaks in the central region around 540 cm^{-1} (67 meV). For NMMO, in this region, a shift of the peak intensity in the Raman spectra towards higher wavenumbers, *i.e.* higher energies, can be observed upon charging. A corresponding slight blueshift is also picked up by the center of gravity of the RIXS peak shifting towards higher energy loss. In LR-NMC, the same region sees a decrease of the strongest Raman peak, which is consistent with a slight redshift of the center of gravity of the RIXS peak. Moreover, the vibrational progression allows us to gain further insight into the electron–phonon coupling of these materials. A deeper analysis of this is presented further below in Section 2.8.

We point out that both progressions are coupled to electronic excitations appearing at higher energy losses. The shaded areas in Fig. 2 reveal how the evolution of sharp vibrational features is accompanied by changes in the electronic structure, whereby excitation at energy C (bottom panels) predominantly probes bulk-lattice oxygen. Upon charging to EOC (blue lines, shading), both NMMO and LR-NMC exhibit an enhancement and broadening of the main oxygen band, alongside increased intensity in the 2–3 eV (dd-excitations mediated by metal 3d – O 2p hybridization) and >4 eV energy-loss regions. At excitation B (middle panels) newly formed states at intermediate delithiation/desodiation are probed, leading to selective enhancement of the 2–3 eV region, consistent with increased hybridization or charge transfer. These aspects are relevant for the discussion about the evolution of electron–phonon coupling during charging.

3.3 Origin of Progression II

Progression II is unique to the lower energy excitation A (Fig. 2, top panels) with an energy spacing of ~99 meV and is observed only in EOC samples (blue lines). It is notably absent at excitations B and C (middle and bottom panels) and undetected in Raman spectra, presenting an even stronger vibrational response than observed at other energies. Attempts to associate this mode with the O–O stretching vibrations of Na_2O_2 and Li_2O_2 are plausible but fail due to both energetic and spectroscopic mismatch: while the vibrational progression of Li_2O_2 is close in energy spacing at first assumption (~95 meV), the absorption threshold of Li_2O_2 begins near 529 eV with a maximum around 531 eV. Excitation A lies lower centered

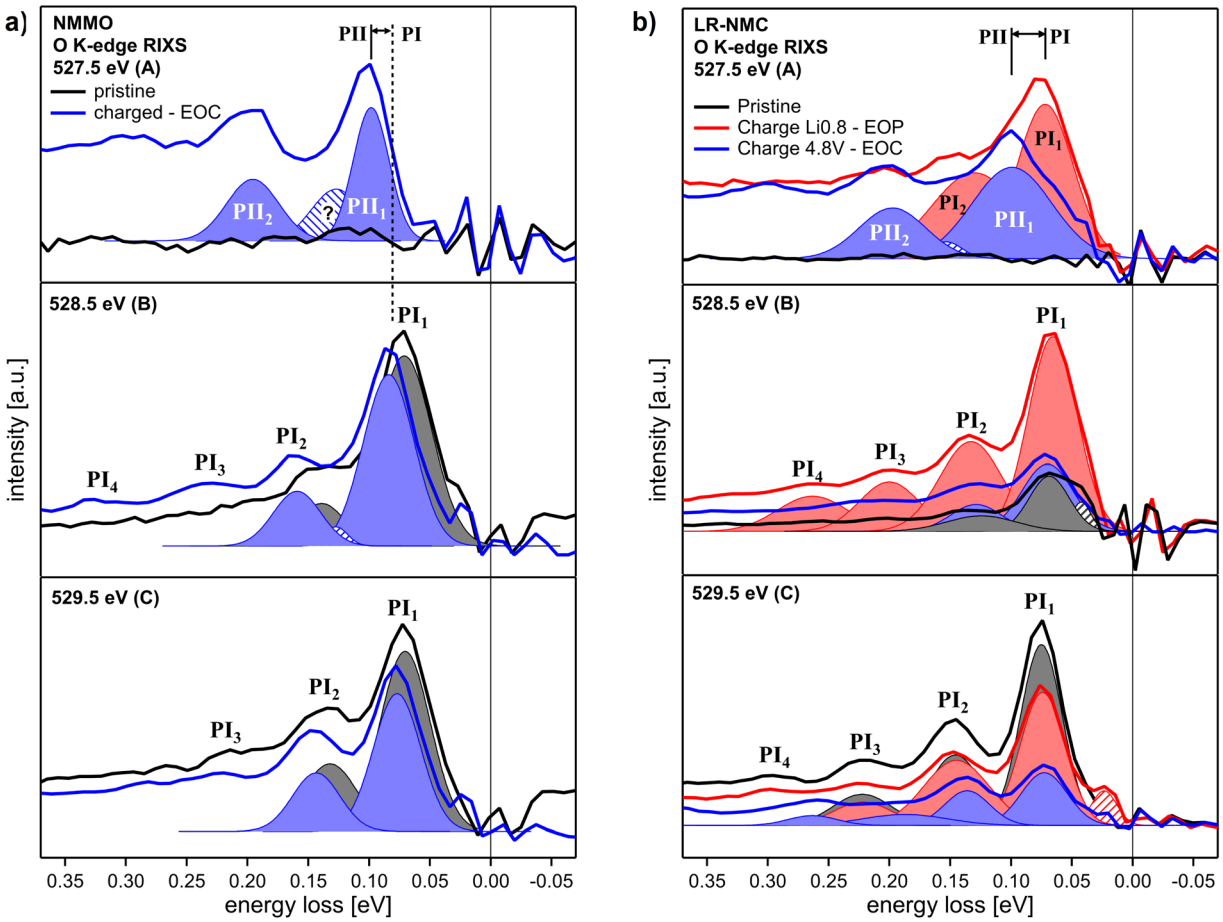

Fig. 3 O K-RIXS on NMMO (a) and LR-NMC (b) at 527.5 (top), 528.5 (middle), and 529.5 eV (bottom). PI and PII refer to Progression I and II respectively, with the index of each indicating the order of the corresponding vibrational peak. The hatched peaks signify peaks that are necessary for a converging peak fit that cannot be clearly assigned to a vibrational progression. The spectra are normalized to the elastic peak which is subsequently subtracted *via* the procedure described in the SI.

around ~527.5 eV, without any visible signal close to the Li_2O_2 resonance. For Na_2O_2, measured peroxide modes exhibit higher fundamental vibrational energies (>125 meV), again above the resonance of excitation A. Corresponding RIXS maps for Li_2O_2 and Na_2O_2 are shown in SI Fig. S8.

Instead, prior studies have reported similar narrow absorption resonances at ~527.5 eV in oxygen-redox systems such as $Na_{0.6}[Li_{0.2}Mn_{0.8}]O_2$ (ref. 17) and $Na_{2-x}Mn_3O_7$,[19] attributed to delocalized hole states and oxygen hole polarons, respectively. In both NMMO and LR-NMC, a more diffuse shoulder appears at this energy (see Fig. 1). In the present study, the RIXS excitation at this shoulder leads to a new vibrational structure distinct from the lattice-coupled Progression I.

Conceivably, electron extraction at high states of charge may lead to stable lattice oxygen hole formation that interact to form polarons. We thus assign Progression II to excitations of polarons formed between oxidized oxygen ions when the cathodes are highly desodiated/delithiated (EOC). These lattice-oxygen holes form states close to the Fermi level, and thus create an absorption that resonates at threshold energies (527.5 eV), distinct from trapped O_2 (531 eV). Alongside the vibrational progression, the delithiated/desodiated cathodes display a pronounced continuum enhancement between 0 and 4 eV (Fig. 2), attributable to electronic excitations. Intriguingly, the strong electron–phonon coupling implied by the vibrational progression contrasts with the broad bandwidth of this continuum, leaving the degree of electronic localization unresolved.

Therefore, the data suggests that while O_2 formation remains the dominating reaction (indicated by its large vibrational intensity compared to the vibrational feature resulting from polarons – see SI Fig. S7), polaronic states can become stabilized at high degrees of delithiation/desodiation, remaining unable to condense into O_2. This could also play a role in the observed lower O_2 formation in NMMO compared to LR-NMC. The two processes of polaron and trapped O_2 formation appear dynamically coupled, suggesting that the polaronic states cannot be observed at lower states of charged using *ex situ* RIXS, due to their rapid decay to trapped O_2. Accordingly, *operando* RIXS measurements are needed to verify this behavior.

We point out that polarons might only form in the core excited state, *i.e.* the excitation initially leads to core excitons

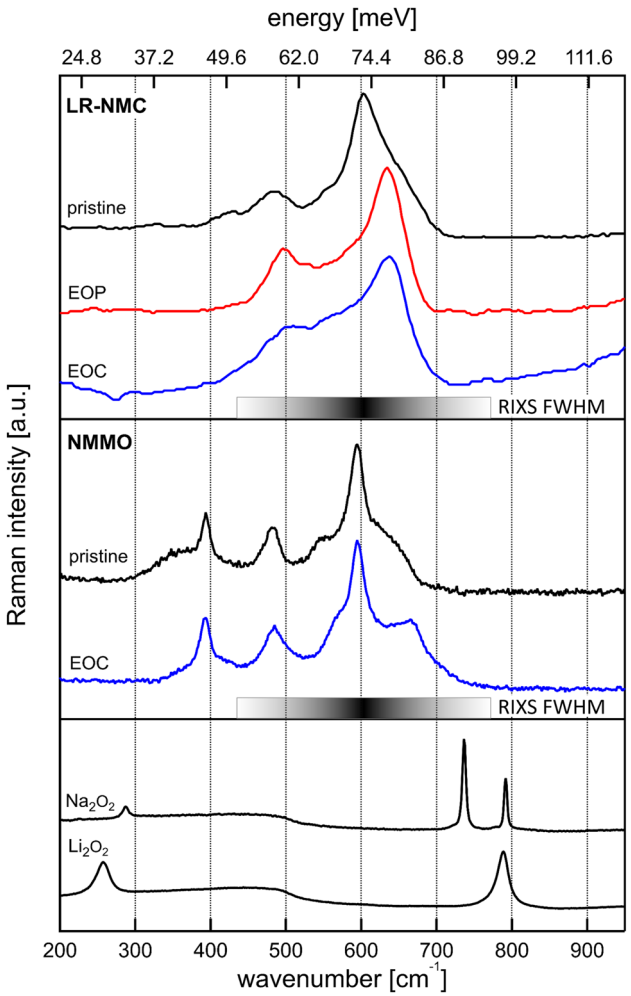

Fig. 4 Raman data of NMMO, and LR-NMC, and peroxide references. The grayscale bar indicates the full width at half maximum (FWHM) of the corresponding vibrational RIXS peak.

that couple to the observed phonon. Alternatively, stable polarons existing in the ground state (before core excitation) cause associated lattice distortions. However, these might be hard to detect with structurally sensitive methods due to the small relative number of participating oxygen ions *e.g.* compared to trapped O_2-formation. Nevertheless, H. Koga *et al.* have reported Mn K-edge of LR-NMC revealing indications of initial cycle distortions in the charged state, possibly related to our observation.[25] Another extensive theoretical study by K. Hoang concluded that *e.g.* "Li_2MnO_3 oxidation of Mn^{3+} to Mn^{4+}, leading to the formation of small hole polarons at the transition-metal site".[26] Thus, our results certainly prompt both future theoretical investigations as well as in depth follow-up RIXS studies to pin point the likely sites of associated lattice distortions.

Progressions I and II thus reveal that, in contrast to the "extrinsic" oxygen-redox signal from trapped-O_2, the absorption structures at the O K-XAS threshold formed upon charging are attributed to intrinsic lattice oxygen responses, *e.g.* by formation of $3d^nL$ and $3d^nL^2$ electronic states, where L is a ligand hole. While beyond the present scope, concentration variation of TM-ions can be crucial for ligand hole behavior. Our present study focuses on Mn-rich cathodes, yet we briefly mention that O K-XAS spectra of oxygen redox related Ni-rich cathodes reveal a similar threshold behavior,[27] while it remains to be investigated whether RIXS also shows similar phonon and polaron formation. Thus, our study points the way to illucidate oxygen hole formation dependencies on *e.g.* TM-covalency and TM-O hybridisation through application of RIXS at the O K-XAS threshold.

3.4 Electron–phonon coupling

Electron–phonon coupling in layered oxide oxygen-redox cathodes could play a pivotal role in their electrochemical behavior and underlying physics. Thus it is crucial to use RIXS to derive direct information about energy positions, phonon peaks widths, and the EPC constant. The shape and intensity ratios of the vibrational progressions observed in the RIXS spectra provide valuable insights into the evolution of the EPC (also referred to as exciton-phonon coupling[23]) within these materials as they are cycled. The coupling strength can be inferred qualitatively from the strength of the vibrational progression and the rate at which its intensity decays with increasing vibrational quantum number.

We recall that Progression I at excitation C is linked to the lattice oxygen vibrations A_{1g} as observed with Raman spectroscopy. Interestingly, the RIXS spectra reveal distinct behavior between NMMO and LR-NMC. In NMMO, only two distinct vibrational peaks are clearly resolved, limiting a detailed analysis of their progression. Nevertheless, the intensity ratio between the first and second vibrational peaks increases upon charging, suggesting an enhancement of electron–phonon coupling in the charged NMMO sample.

In contrast, LR-NMC displays a reduction in the vibrational signature upon charging. Both the overall intensity and the intensity ratio between the first and second vibrational peaks decrease, indicating a weakening of electron–phonon coupling. Interestingly, although LR-NMC exhibits more discernible vibrational peaks (three to four identifiable modes), the intensity drop between the first and second peaks is more rapid than that observed for NMMO. This suggests that NMMO, despite fewer visible peaks, exhibits stronger electron–phonon coupling.

Table 1 Intensity ratio between the first vibrational peak and the main edge feature (≈3.9 eV energy loss) of both LR-NMC and NMMO. The values are taken from the raw RIXS spectra

	LR-NMC			NMMO	
Exc.	pris.	EOP	EOC	pris.	EOC
A	—	1.50	2.34	—	2.03
B	1.16	1.15	0.88	0.94	0.89
C	0.31	0.26	0.29	0.18	0.27

Additionally, as discussed earlier with reference to Fig. 2, the ratio between the low-energy vibrational features (<100 meV) and the main RIXS peak (~3.9 eV energy loss) serves as a first indicator of electron–phonon coupling strength. Table 1 summarizes these ratios for all three excitation energies. At excitation A, the vibrational feature is particularly prominent, surpassing the main RIXS peak in both charged NMMO and LR-NMC samples. At excitation C, the ratios are smaller, however, a trend can be observed between the pristine and EOC samples in both materials. For NMMO, the intensity ratio increases upon charging, while for LR-NMC we observe a slight decrease in ratio.

To further substantiate these observations, theoretical modeling following the approach described by Gilmore *et al.*[23] was performed as described in Section 2.8. Phonon excitation models were fitted to the experimental RIXS spectra at excitation C, as shown in Fig. 5. From these fits, the electron–phonon coupling constant M_{epc}, the phonon excitation energy ω_{ph}, and the inverse phonon lifetime Γ_{ph} were extracted. The resulting parameters are listed in Table 2.

During the fitting, the detuning energy relative to the phonon resonance ($\omega_{det} = \omega_{ex} - \omega_{in}$) was set to zero, as the precise resonance energy could not be independently determined and is assumed to be close to the selected RIXS excitation energies. If detuning were present, the extracted M_{epc} values would represent lower bounds.

The fitted ω_{ph} align well with the values obtained from the earlier multipeak fitting shown in Fig. 3. The phonon lifetimes, characterized by $\Gamma_{ph}/2$, are larger for NMMO than for LR-NMC, although the uncertainties ranging from 20% (pristine NMMO) to 70% (pristine LR-NMC) limit quantitative comparison.

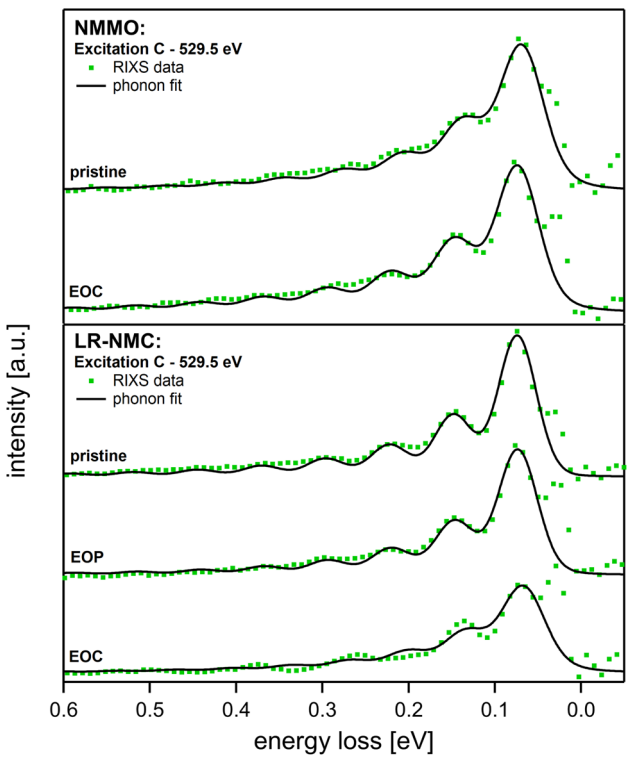

Fig. 5 O K-RIXS on NMMO (top) and LR-NMC (bottom) at excitation C (529.5 eV). The vibrational progressions were fitted to analyze the phonon excitations in the range between 0.041 to 0.45 eV energy loss.

Table 2 Calculated values for M_{epc}, ω_{ph}, and $\Gamma_{ph}/2$ from the fitting procedure displayed in Fig. 5. For this fitting procedure $\gamma = 240$ meV[28] was chosen. Values marked with an asterisk indicate a difficulty with the fitting procedure described in the text

	LR-NMC			NMMO	
[meV]	pris.	EOP	EOC	pris.	EOC
M_{epc}	136(6)	128(4)	139(11)*	168(8)	152(6)
ω_{ph}	74.5(6)	73.7(6)	67(1)*	69(1)	74.0(7)
$\Gamma_{ph}/2$	0.4(3)	0.9(6)	6(2)*	7(2)	4(1)

For LR-NMC, the pristine sample exhibits an M_{epc} of 136(6) meV, which decreases to 128(4) meV in the EOP sample. Fitting the fully charged (EOC) LR-NMC sample proved challenging due to irregularities in the vibrational peak structure; the fitted M_{epc} value of 139(11) meV carries an uncertainty roughly twice as large as the pristine and EOC samples. These difficulties likely arise from the presence of overlapping vibrational modes, one centered around 70 meV and another near 150 meV. This becomes apparent when examining the third (~200 meV) and fourth (~270 meV) vibrational peaks, where the third peak vanishes and the fourth reappears, an effect consistently observed across two independent measurements (70° and 154° scattering geometries, see SI Fig. S3).

In NMMO, the pristine and charged samples could be fitted reliably, yielding M_{epc} values of 168(8) meV (pristine) and 152(6) meV (charged), respectively. Comparing the two materials, the pristine NMMO sample exhibits a higher M_{epc} than pristine LR-NMC. Upon charging, the electron–phonon coupling decreases in both NMMO and LR-NMC, while NMMO retains a higher M_{epc} than LR-NMC. Importantly, one fixed parameter during the fitting procedure is the inverse core-hole lifetime of the intermediate state γ, the value of which impacts the resulting M_{epc} significantly. The chosen value for γ used for the calculated values shown in Table 2 was 240 meV, based on the work done by Vale *et al.*[28] who calculated γ for a comparable material Li_2IrO_3. To give an idea of possible M_{epc} depending on varying values of γ, we test upper and lower bounds of γ for the O K-edge from literature: 150 meV[29–31] for the lower bound, and 300 meV[32] for the upper bound. The resulting values for M_{epc} are seen in Table 3.

Table 3 M_{epc} range acquired by varying γ between 150 to 300 meV for each sample

Sample	M_{epc} range [meV]
LR-NMC pristine	89–170
LR-NMC EOP	83–161
LR-NMC EOC	89–174
NMMO pristine	113–210
NMMO EOC	95–191

The obtained M_{epc} values are consistent with literature reports for similar transition-metal oxides. For instance, Vale *et al.*[28] reported M_{epc} = 170(20) meV for the Ir–O mode in α-Li_2IrO_3, while larger values of $M_{epc} \approx$ 240 meV and 250 meV were reported for Li_2CuO_2 (ref. 33) and $BaTiO_3$,[34] respectively. Finally, electron–phonon coupling constants extracted from phonon progressions track redox-induced bond reorganisation and differ qualitatively between Na- and Li-based cathodes. Probing electron–phonon coupling offers a direct window into how charge and lattice motions intertwine during oxygen redox in layered-oxide cathodes. Our analysis thus presents a new pathway to gain deeper insight into the effects of oxygen redox.

In summary, our observations paint an interesting picture about oxygen redox dynamics in these two systems. Primarily, oxygen redox leads to trapped O_2 in both systems but other forms of competing oxygen are present as well, namely formation of lattice-oxygen holes that form polarons. These appear to become energetically favorable at the end of charge and might signify a limiting factor for continued trapped O_2 production. However, importantly, the signal intensity of the trapped O_2 signal at ~531 eV is significantly stronger than that resulting from polaron formation (as shown in the SI, Fig. S7). It is interesting to note that NMMO forms relatively less O_2 than LR-NMC and shows a stronger and purer polaron-mode at 98 meV. The quicker build-up of occupied states close to the Fermi level seen in RIXS of NMMO could be a tell-tale sign for this process, as well as the weaker development of occupied states close to the Fermi level at incident energy B, possibly blocking a more effective pathway for formation of stable trapped O_2 for storing energy in anionic transformations.

4 Conclusion

We observe two previously unresolved sets of vibrational progressions in the oxygen redox battery cathode materials NMMO and LR-NMC. We attribute these signatures to lattice phonons that strongly couple to certain electronic excitations emerging simultaneously. We determine the coupling constant M_{epc} by a numerically fitting procedure and find it to be comparable to other transition-metal oxide battery cathode materials.

The fundamental frequency of the first progression (68–84 meV) is found to match previously found Raman spectroscopy shifts in both pristine and charged states and the enhanced electronic states are in the energy loss range typical for Mn dd-excitations (2–3 eV). The phonon energies show a sensitivity on the state of charge of the cathodes that is consistent with Raman spectroscopy results.

The second vibrational progression belongs to a completely novel OR process observed in these materials that has only been possible to distinguish from the overwhelming O_2-formation thanks to the excitation energy discrimination afforded by the RIXS process. It manifests itself by a 98–99 meV fundamental mode that emerges only at the EOC, coinciding with the culmination of the trapped-O_2 oxygen-redox signature of the cathodes. Simultaneously, a broad continuum of occupied, apparently delocalized electronic states develops near the Fermi level, providing the first clear evidence of an intrinsic lattice-oxygen redox effect. Our analysis suggests that these excitations arise from polarons formed between neighboring oxidized oxygen ions under deep desodiation/delithiation. It is conceivable that at lower states of charge, lattice-oxygen holes rapidly evolve into trapped O_2, thus evading detection in *ex situ* RIXS – a hypothesis warranting future *operando* studies.

Conflicts of interest

The authors declare no conflict of interest.

Data availability

All data related to this study is included in the figures contained in this article. Supplementary information (SI): corresponding raw data, as well as a description of the elastic peak subtraction, data fitting procedures, and comparisons to other RIXS signals (O_2 *vs.* polaron, Li_2O_2 and Na_2O_2 maps). See DOI: https://doi.org/10.1039/d5ta07689g.

Acknowledgements

The authors acknowledge financial support from the Swedish Energy Agency to the project "X-ray based methodology for next generation Na-ion battery cathodes" (project number: 50745-1) and project P2021-90225, as well as the Swedish research council (project number: 2023-05072 and 2018-06465).

References

1 A. Manthiram, *Nat. Commun.*, 2020, **11**, 1550.
2 J. M. Tarascon and M. Armand, *Nature*, 2001, **414**, 359–367.
3 J. B. Goodenough and K. S. Park, *J. Am. Chem. Soc.*, 2013, **135**, 1167–1176.
4 J. B. Goodenough and Y. Kim, *Chem. Mater.*, 2010, **22**, 587–603.
5 Z. Lu and J. R. Dahn, *J. Electrochem. Soc.*, 2002, **149**, A815.
6 S. Muhammad, H. Kim, Y. Kim, D. Kim, J. H. Song, J. Yoon, J. H. Park, S. J. Ahn, S. H. Kang, M. M. Thackeray and W. S. Yoon, *Nano Energy*, 2016, **21**, 172–184.
7 H. Koga, L. Croguennec, M. Ménétrier, P. Mannessiez, F. Weill and C. Delmas, *J. Power Sources*, 2013, **236**, 250–258.
8 H. Koga, L. Croguennec, M. Ménétrier, K. Douhil, S. Belin, L. Bourgeois, E. Suard, F. Weill and C. Delmas, *J. Electrochem. Soc.*, 2013, **160**, A786–A792.
9 G. Assat, A. Iadecola, D. Foix, R. Dedryvere and J. M. Tarascon, *ACS Energy Lett.*, 2018, **3**, 2721–2728.
10 D. H. Seo, J. Lee, A. Urban, R. Malik, S. Kang and G. Ceder, *Nat. Chem.*, 2016, **8**, 692–697.
11 K. Luo, M. R. Roberts, R. Hao, N. Guerrini, D. M. Pickup, Y. S. Liu, K. Edström, J. Guo, A. V. Chadwick, L. C. Duda and P. G. Bruce, *Nat. Chem.*, 2016, **8**, 684–691.
12 J. J. Marie, R. A. House, G. J. Rees, A. W. Robertson, M. Jenkins, J. Chen, S. Agrestini, M. Garcia-Fernandez, K. J. Zhou and P. G. Bruce, *Nat. Mater.*, 2024, **23**, 818–825.

13 X. Gao, B. Li, K. Kummer, A. Geondzhian, D. A. Aksyonov, R. Dedryvère, D. Foix, G. Rousse, M. B. Yahia, M. L. Doublet, A. M. Abakumov and J. M. Tarascon, *Nat. Mater.*, 2025, **24**, 743–752.
14 K. McColl, S. W. Coles, P. Zarabadi-Poor, B. J. Morgan and M. S. Islam, *Nat. Mater.*, 2024, **23**, 826–833.
15 A. Menon, B. Johnston, S. Booth, L. Zhang, K. Kress, B. Murdock, G. P. Fajardo, N. Anthonisamy, N. Tapia-Ruiz, S. Agrestini, M. Garcia-Fernandez, K. Zhou, P. Thakur, T. Lee, A. Nedoma, S. Cussen and L. Piper, *PRX Energy*, 2023, **2**, 013005.
16 R. A. House, H. Y. Playford, R. I. Smith, J. Holter, I. Griffiths, K. J. Zhou and P. G. Bruce, *Energy Environ. Sci.*, 2022, **15**, 376–383.
17 R. A. House, U. Maitra, M. A. Pérez-Osorio, J. G. Lozano, L. Jin, J. W. Somerville, L. C. Duda, A. Nag, A. Walters, K. J. Zhou, M. R. Roberts and P. G. Bruce, *Nature*, 2020, **577**, 502–508.
18 M. Hirsbrunner, A. Mikheenkova, P. Törnblom, R. A. House, W. Zhang, T. C. Asmara, Y. Wei, T. Schmitt, H. Rensmo, S. Mukherjee, M. Hahlin and L. C. Duda, *Phys. Chem. Chem. Phys.*, 2024, **26**, 19460–19468.
19 I. I. Abate, C. D. Pemmaraju, S. Y. Kim, K. H. Hsu, S. Sainio, B. Moritz, J. Vinson, M. F. Toney, W. Yang, W. E. Gent, T. P. Devereaux, L. F. Nazar and W. C. Chueh, *Energy Environ. Sci.*, 2021, **14**, 4858–4867.
20 U. Maitra, R. A. House, J. W. Somerville, N. Tapia-Ruiz, J. G. Lozano, N. Guerrini, R. Hao, K. Luo, L. Jin, M. A. Pérez-Osorio, F. Massel, D. M. Pickup, S. Ramos, X. Lu, D. E. McNally, A. V. Chadwick, F. Giustino, T. Schmitt, L. C. Duda, M. R. Roberts and P. G. Bruce, *Nat. Chem.*, 2018, **10**, 288–295.
21 K. J. Zhou, A. Walters, M. Garcia-Fernandez, T. Rice, M. Hand, A. Nag, J. Li, S. Agrestini, P. Garland, H. Wang, S. Alcock, I. Nistea, B. Nutter, N. Rubies, G. Knap, M. Gaughran, F. Yuan, P. Chang, J. Emmins and G. Howell, *J. Synchrotron Radiat.*, 2022, **29**, 563–580.
22 K. Gilmore and A. Geondzhian, *RIXS.phonon*, https://github.com/geonda/rixs.phonons, accessed: 12.12.2025.
23 K. Gilmore, *Phys. Chem. Chem. Phys.*, 2023, **25**, 217–231.
24 L. J. P. Ament, M. van Veenendaal and J. van den Brink, *Europhys. Lett.*, 2011, **95**, 27008.
25 H. Koga, L. Croguennec, M. Ménétrier, P. Mannessiez, F. Weill, C. Delmas and S. Belin, *J. Phys. Chem. C*, 2014, **118**, 5700–5709.
26 K. Hoang, *Phys. Rev. Appl.*, 2015, **3**, 024013.
27 F.-M. Wang, L. Merinda, N.-H. Yeh, R. A. Yuwono, H.-H. Hsia, C. Khotimah and N.-L. Wu, *Nanoscale*, 2025, **17**, 17033.
28 J. G. Vale, C. D. Dashwood, E. Paris, L. S. Veiga, M. Garcia-Fernandez, A. Nag, A. Walters, K. J. Zhou, I. M. Pietsch, A. Jesche, P. Gegenwart, R. Coldea, T. Schmitt and D. F. Mcmorrow, *Phys. Rev. B*, 2019, **100**, 224303.
29 O. Björneholm, M. Bässler, A. Ausmees, I. Hjelte, R. Feifel, H. Wang, C. Miron, M. Piancastelli, S. Svensson, S. Sorensen, *et al.*, *Phys. Rev. Lett.*, 2000, **84**, 2826.
30 V. Carravetta, *et al.*, *Phys. Rev. A*, 1987, **35**, 1022.
31 R. Sankari, M. Ehara, H. Nakatsuji, Y. Senba, K. Hosokawa, H. Yoshida, A. De Fanis, Y. Tamenori, S. Aksela and K. Ueda, *Chem. Phys. Lett.*, 2003, **380**, 647–653.
32 F. Frati, M. O. Hunault and F. M. De Groot, *Chem. Rev.*, 2020, **120**, 4056–4110.
33 S. Johnston, C. Monney, V. Bisogni, K. J. Zhou, R. Kraus, G. Behr, V. N. Strocov, J. Málek, S. L. Drechsler, J. Geck, T. Schmitt and J. V. D. Brink, *Nat. Commun.*, 2016, **7**, 10563.
34 S. Fatale, S. Moser, J. Miyawaki, Y. Harada and M. Grioni, *Phys. Rev. B*, 2016, **94**, 195131.